H-MINT: MODELING POCKET-LIGAND BINDING WITH HIERARCHICAL MOLECULAR INTERACTION NETWORK

Anonymous authors
Paper under double-blind review

ABSTRACT

Accurate molecular representations are critical for drug discovery, and a central challenge lies in capturing the chemical environment of molecular fragments, as key interactions, such as H-bond and π stacking—occur only under specific local conditions. Most existing approaches represent molecules as atom-level graphs; however, individual atoms cannot express stereochemistry, lone pairs, conjugation, and other complex features. Fragment-based methods (*e.g.*, principal subgraph or functional group libraries) fail to preserve essential information such as chirality, aromatic bond integrity, and ionic states. This work addresses these limitations from two aspects. (i) **OverlapBPE tokenization**[1]. We propose a novel data-driven molecule tokenization method. Unlike existing approaches, our method allows overlapping fragments, reflecting the inherently fuzzy boundaries of small-molecule substructures and, together with enriched chemical information at the token level, thereby preserving a more complete chemical context. (ii) **h-MINT model**. We develop a hierarchical molecular interaction network capable of jointly modeling drug–target interactions at both atom and fragment levels. By supporting fragment overlaps, the model naturally accommodates the many-to-many atom–fragment mappings introduced by the OverlapBPE scheme. Extensive evaluation against state-of-the-art methods shows our method improves binding affinity prediction by 2-4% Pearson/Spearman correlation on PDBBind and LBA, enhances virtual screening by 1-3% in key metrics on DUD-E and LIT-PCBA, and achieves the best overall HTS performance on PubChem assays. Further analysis demonstrates that our method effectively captures interactive information while maintaining good generalization.

1 INTRODUCTION

Precise modeling of protein-ligand interactions is pivotal for fundamental tasks, such as binding affinity prediction and virtual screening, in early-stage drug discovery (R Laurie & Jackson, 2006). To accurately decipher these interactions, it is essential to build expressive representations to fully capture the chemical environment of the molecules. Most existing methods represent molecules as atom-level graphs (Zhou et al., 2023); however, it is questionable whether they are able to learn essential chemical information (*e.g.*, stereochemistry, lone pairs, conjugation) just from atomic tokens (Wigh et al., 2022). Another line of work employs molecular fragmentation (*e.g.*, Principal Subgraph (Kong et al., 2022b)) to preserve local contexts for atoms, in accordance with the intuition that many physicochemical properties occur at the fragment level (Murray & Rees, 2009). Nevertheless, these methods still fail to preserve crucial information like chirality, aromatic bond integrity, and ionic states, which stems from their naive partitioning of molecules into disjoint sets.

This work addresses the above limitations by integrating innovations in both molecular representations and model architectures. (i) We propose a novel and frequency-based molecular tokenization (*i.e.*, fragmentation) algorithm, **OverlapBPE**, which preserves essential chemical knowledge (*e.g.*, chirality, aromaticity, charges). Specifically, we enrich the atomic representation with their properties (*e.g.*, charges) and further incorporate 3D conformations during an iterative tokenizing process to extract frequently occurring fragments. To maintain the integrity of aromatic systems, we further enable

[1]BPE (Byte Pair Encoding) (Sennrich et al., 2016) is a statistical tokenization method that iteratively merges the most frequent pairs of symbols in a corpus to generate compact and efficient subword units.

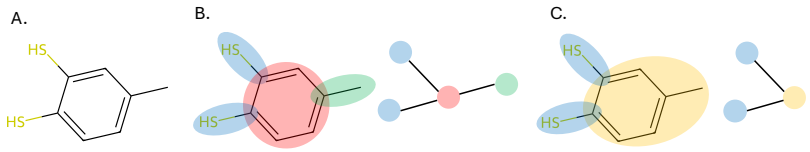

Figure 1: **Illustration of the OverlapBPE tokenization process**. (i) Starting from the molecule in A, we first extract all basic tokens from the atom graph. (ii) After identifying all basic tokens, we obtain the initial fragments (left) and token graph (right), as shown in B, which contains 4 tokens in 3 types: `c1ccccc1` (freq=3778), `Cc` (freq=3496), and `Sc` (freq=637). (iii) We then enumerate all adjacent token pairs and identify the highest-frequency composite token from the final vocabulary Φ_{final}, namely `Cc1ccccc1` (freq=2458). (iv) Merging `c1ccccc1` and `Cc` into a new token, we obtain new fragments and token graph, as shown in C, containing 3 tokens in 2 types: `Cc1ccccc1` (freq=2458), `Sc` (freq=637). (v) Continue enumerating adjacent pairs in token graph C; no matched token found in vocabulary, the algorithm terminates.

atom overlaps between mined fragments, leading to a many-to-many mapping between atoms and fragments. For example, a Naphthalene (`c1c2ccccc2ccc1`) can be tokenized into 2 benzene rings (`c1ccccc1`) that share 2 aromatic C atoms. While the many-to-many mapping is necessary for aromatic integrity, it also poses an additional challenge on the model architecture, as most existing hierarchical molecular networks only support 1-1 mapping between atoms and fragments. (ii) To support our OverlapBPE tokenization, we build the hierarchical Molecular Interaction NeTwork (**h-MINT**), which explicitly accommodates the many-to-many atom–fragment mapping. h-MINT introduces a bilevel attention mechanism that allows bidirectional information flow between atoms and overlapping fragments, and further expands fragment-level relations into atom-level geometric edges. This hierarchical yet equivariant design enables the model to capture multi-scale interaction patterns while maintaining global consistency.

Extensive experiments exhibit the superiority of our method over existing baselines, highlighting 2-4% performance gains on Pearson/Spearman correlation for binding affinity prediction, 1-3% gains on key metrics for virtual screening, and the best overall performance in HTS. Further analysis shows that our tokenization captures important inductive bias, making our model robust to noise and maintaining good generalization under different settings, indicating great potential for real-world applications.

2 Background and Related Work

Fragment-Based Molecular Tokenization Fragmentation partitions atom-level molecular graph into coarse units that captures meaningful substructural features. Early work relied on hand-crafted junction-tree rules or predefined fragment libraries (Jin et al., 2018; 2020; Yang et al., 2021). To reduce manual bias, subsequent studies adopted unsupervised frequent-subgraph mining to construct fragmentation rules in a data-driven manner: the underlying search is NP-hard (Kuramochi & Karypis, 2001; Jazayeri & Yang, 2021), but approximate algorithms make it tractable in practice (Inokuchi et al., 2000; Yan & Han, 2002; Nijssen & Kok, 2004; Geng et al., 2023). Byte-pair encoding (BPE), which iteratively merges the most frequent token pairs to build a compact vocabulary, has also been adapted to 2D molecular data (Li & Fourches, 2021; Ucak et al., 2023; Shen & Póczos, 2024). Our work is closely related to PS-VAE (Kong et al., 2022b), which proposes a data-driven tokenization that automatically mines and merges the most frequent, maximally-sized molecular fragments (*i.e.*, *principal subgraph*). However, essential chemical information, such as stereochemistry and conjugation, is usually neglected. In contrast, our proposed OverlapBPE tackles these challenges by enriching atomic properties, involving 3D stereochemistry, and enabling overlapping between fragments.

Molecular Interaction Modeling Recent deep-learning frameworks for biomolecular modeling seek to couple fine-grained molecular representations interacting at multiple spatial resolutions. At the finest scale, atom-level graphs are usually processed with $E(n)$-equivariant or directional message-passing networks, capturing local physics with high fidelity (Schütt et al., 2017; Satorras et al., 2021; Xu et al., 2022; Hoogeboom et al., 2022; Atz et al., 2021; Zaidi et al., 2022; Townshend et al., 2020). To reason over chemistry that spans several bonds such as aromatic conjugation,

hydrogen-bond lattices and π-stacking, researchers introduce coarser views by pooling atoms into residues or surfaces for proteins (Jin et al., 2022; Anand & Achim, 2022; Somnath et al., 2021; Wang et al., 2022), dual graphs for inverse folding (Gao et al., 2022), and functional-groups mined from small-molecule graphs (Jin et al., 2018; Kong et al., 2022b; Geng et al., 2023). Cross-molecule modules then embed ligand and receptor in a shared 3-D frame and predict poses or affinities with regression, contrastive, or diffusion objectives (Kong et al., 2022a; Luo et al., 2022; Stärk et al., 2022; Kong et al., 2024; Gao et al., 2023). Although these approaches broaden the receptive field, they often remain confined to a single resolution and are unable to enable bidirectional information flow between atoms and their corresponding substructures. Compared with prior hierarchical GNN approaches, our h-MINT introduces an atom–token overlap mechanism and expands token-level relations into atom-level geometric edges, enabling more flexible cross-scale information flow and yielding fine-grained yet globally consistent interaction modeling.

3 METHODOLOGY

3.1 OVERLAPBPE TOKENIZATION

We reveal that the failures of existing fragment-based methods stem from the naive partitioning of molecules into disjoint sets. To address these limitations, we propose a new tokenization approach that permits atom overlaps between mined fragments, enabling more expressive, coherent, and chemically meaningful molecular representations.

Atom Graph An atom graph can be represented as a property graph $G^a = (V^a, E^a)$, where $V^a = \{a_i\}$ is a set of atoms, $E^a \subset V^a \times V^a$ is the set of bonds, and each atom/bond has an associated element/bond type. A tokenization step maps a subgraph of G^a with certain atoms and bonds into a **token** $(V', E') \to f \in \Phi$, where $(V', E') = G^a[V'] \subset 2^V \times 2^E$ is an induced subgraph, and Φ is the set of tokens.

Token Graph A token graph G^f is constructed from an atom graph G^a through contracting subgraphs in G^a as a single node while preserving connectivity. To guarantee not breaking important substructures and support token overlap, we first identify a set of **basic tokens** Φ_{basic}, which includes smallest fragments that are chemically meaningful and should be preserved during partitioning. We include all single atoms, bonds, and rings collected from the training set in Φ_{basic}[2] to guarantee the token set is complete, yet not all of the basic tokens will be added to the final vocabulary. In practice, we first replace all rings with tokens, then bonds, and lastly atoms to make sure all atoms and bonds are covered in the token graph G^f. In G^f, each node is a basic token, and the tokens are connected through sharing atoms (or disconnected when it is an ion).

$$G^f = (V^f, E^f), \quad \mathcal{T}^f : V^f \to \Phi_{\text{basic}} \tag{1}$$

where V^f is the set of tokens, $E^f \subseteq V^f \times V^f$ encodes their adjacency (*e.g.*, two tokens share atoms or connected by bonds), and $\mathcal{T}^f$ maps each fragment node to its token type in Φ_{basic}. Besides, the following tokenization process follows a bottom-up BPE merge fashion[3], which also guarantees that the basic tokens will not be broken.

Frequency-Based Vocabulary Setup After we get the token graph G^f consisting of basic tokens, we iteratively discover new **composite tokens** and update the vocabulary Φ_{comp} as follows:

1. For a given token graph $G^f = (V^f, E^f)$, enumerate all adjacent fragment pairs $(f_i, f_j) \in E^f$ as composite token candidates: $\mathcal{C} = \{\text{Merge}(f_i, f_j) \mid (f_i, f_j) \in E^f\}$ where $\text{Merge}(f_i, f_j)$ denotes the operation of combining two neighboring fragments into a larger fragment. Token frequency is computed over the training corpus.
2. Select the most frequent token $f^* \in \mathcal{C}$ and add it to the vocabulary: $\Phi_{\text{comp}} \leftarrow \Phi_{\text{comp}} \cup \{f^*\}$.

[2]Aromatic rings are treated as single delocalized π systems to preserve conjugation.

[3]In BPE, tokenization starts from an initial vocabulary of basic tokens (*e.g.*, characters or word pieces), and iteratively merges the most frequent adjacent pairs. Since merging only combines existing tokens without splitting them, the original basic tokens remain intact.

3. Update all fragment graphs $\{G^f\}$ in the corpus by replacing each occurrence of f^* with a new hyper node. Note that the original fragments in V^f will not be removed from G^f unless all of its adjacent composite candidates have been merged.
4. Repeat steps 1–3 until a stopping criterion (*e.g.*, iteration steps) is met.
5. Filter Φ_{basic} and Φ_{comp} with minimum frequency threshold to make sure a proper vocabulary size $\Phi_{\text{final}} = \{f \in \Phi_{\text{basic}} \cup \Phi_{\text{comp}} | \text{freq}(f) > t\}$.

OverlapBPE Tokenization After obtaining the vocabulary, we can tokenize an atom-bond graph G^a following the frequency of tokens in Φ_{final}. Figure 1 illustrates the tokenization process.

1. Find all basic tokens Φ_{basic} from G^a and convert G^a into fragment graph G^f. For basic tokens in G^f, we preserve their token identifier if it's in Φ_{final}, otherwise, we replace it with a special identifier (*e.g.*, <ring>) to make sure not breaking it in the following.
2. For G^f, enumerate all adjacent fragment pairs $(f_i, f_j) \in E^f$ and find the matching token $f^* \in \Phi_{\text{final}}$ with the highest frequency that can be merged from pair(s) $(f_i, f_j) \in E^f$. Replace pair(s) with f^* and update G^f. Note that a token $f_i \in N^f$ will not be removed from G^f unless f_i and all its adjacent pairs $(f_i, f_j) \in E^f$ have been merged.
3. Repeat step 2 until no fragment pairs match tokens in Φ_{final}.

Chemical Information Incorporation Our vocabulary can be easily extended to incorporate domain knowledge. (i) To distinguish **Chirality**, the algorithm operates on 2D molecular graphs augmented with 3D conformer information. The use of 3D coordinates ensures that stereochemistry is preserved during tokenization. As a result, each token is assigned a unique isomeric SMILES string as its vocabulary identifier, encoding both atomic connectivity and chirality. For example, L-lactic and R-lactic are represented by `C[C@H](O)C(=O)O` and `C[C@@H](O)C(=O)O`, respectively. (ii) **Aromatic integrity** is ensured by two complementary mechanisms. First, aromatic rings are treated as indivisible basic tokens, which are preserved throughout the bottom-up merge process. Second, the overlapping tokenization strategy allows for progressive merging of neighboring tokens, enabling the discovery of extended conjugated systems while maintaining aromatic consistency. (iii) To properly encode **atomic attributes**, such as charged and aromatic atoms, we assign explicit identifiers to atoms with formal charges and/or aromatic participation. For instance, `[Cl-]` denotes a negatively charged chlorine atom, while `[n+]` indicates a positively charged aromatic nitrogen. In contrast to standard SMILES, which often omit such details when representing isolated atoms, our token identifiers explicitly preserve these chemically significant properties.

3.2 H-MINT

In this section, we introduce hierarchical Molecular Interaction NeTwork (h-MINT), an SE(3)-equivariant graph Transformer that (i) adapts its self-attention, feed-forward, and normalization layers to maintain equivariance, and (ii) preserves atom–token overlap, allowing atoms to belong to multiple tokens (and vice versa) for flexible fragment representations. The overall architecture is in Figure 2.

3.2.1 Model Input and Embedding

The model receives a pocket-ligand pair as input, including their atoms (V_p^a, V_l^a)[4], tokens (V_p^f, V_l^f), and atom-token mapping $\mathcal{T}_p \subseteq V_p^a \times V_p^f$, $\mathcal{T}_l \subseteq V_l^a \times V_l^f$. Note that: (i) each node in V^a or V^f has a type (*e.g.*, element type `N`, token type `[Cl-]`). (ii) The mapping function $\mathcal{T}$ has 2 parts to map an atom index to its associated token indices $\mathcal{T}_{a2f}$ and vice versa $\mathcal{T}_{f2a}$, yet do not operate on atom and token types. Thus, the embeddings can be obtained:

$$H_p^0 = \text{Embed}(V_p^a, V_p^f, \mathcal{T}_p), \quad H_l^0 = \text{Embed}(V_l^a, V_l^f, \mathcal{T}_l), \tag{2}$$

$$H^0 = \text{Embed}(V^a) + \text{ScatterMean}(\text{Embed}(V^f), \mathcal{T}_{f2a}) + \text{Embed}(\text{Pos}(V^a)), \tag{3}$$

where we use `scatter_mean` to aggregate an atom's associated token types information, and $\text{Pos}(\cdot)$ simply maps an atom to its position code[5] To collect global information from atoms and

[4]We use subscript $_p$ and $_l$ for pocket and ligand, superscript ^{a} and ^{f} to distinguish atom and token (fragment).

[5]The position code for a residue atom is its atom name, *e.g.*, `CA` → `A`, for a molecular atom is a special token <sm>. We leave the complete position code table in the Appendix A.1.

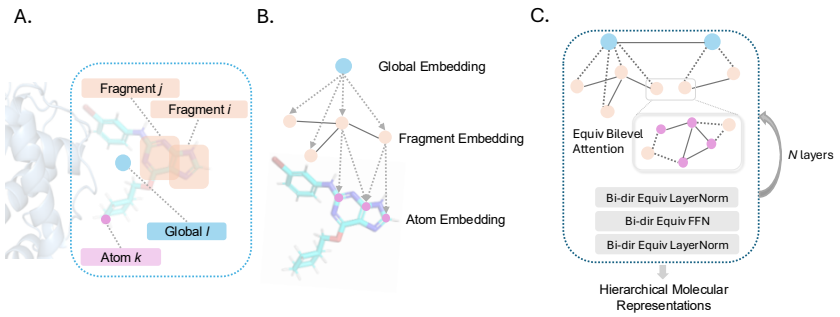

Figure 2: **Overall model architecture**. (A) Global node, fragment tokens, and atoms in the ligand molecule of an input pair. (B) The aggregation of fragment and global embeddings. (C) An encoder layer of h-MINT. *Note*: Solid lines indicate connection within the same level. Dashed lines indicate connections across different levels.

tokens, we also augment special `<global>` tokens to all node lists $V_p^a, V_l^a, V_p^f, V_l^f$. Some example inputs can be found in the Appendix A.1.

3.2.2 Building Hierarchical Graph

The embedding layer only encodes type and position information, and also uses $\mathcal{T}_p, \mathcal{T}_l$ to map token type embedding into atom embedding dimensions. In this section, we further consider 3D structures and build hierarchical graphs for message passing, as shown in Figure 2 B. Before we start building the graph, we need to specify that the edges are directed, which means for any token-level edge (f_i, f_j) or atom-level edge (a_i, a_j), the former node will receive a message from the latter.

KNN Token Graph In the token level, every pair of input contains a sequence of pocket tokens and a sequence of ligand tokens, plus 2 augmented global tokens, as follows:

$$[V_p^f; V_l^f] = [f_{p,g}, f_{p,0}, f_{p,1}, f_{p,2}, \ldots, f_{l,g}, f_{l,0}, f_{l,1}, f_{l,2}, \ldots], \tag{4}$$

where we use f_p and f_l to represent pocket and ligand tokens, and subscription $f_{,g}$ and $f_{,i}$ to denote corresponding global token and i-th token. In this step, we construct a KNN graph for non-global tokens, where the distance between token f_i and f_j is the minimum distance between all their atoms,

$$\text{dist}(f_i, f_j) = \min_{a_s \in f_i, a_t \in f_j} \text{dist}(a_s, a_t), \tag{5}$$

For the two global tokens, we connect them with their following tokens to aggregate information within each pocket and ligand, and we connect the 2 global tokens to exchange pair information. Therefore we get the set of edges $E^f_{\text{KNN}} = \{(f_i, f_j) | f_i \in V_p^f \cup V_l^f, f_j \in \text{KNN}(f_i)\} \cup \{(f_{,g}, f_{,i}) | f_{,i} \in V^f\} \cup \{(f_{p,g}, f_{l,g})\}$. For simplicity, we use $\text{KNN}(f_i) = \{f_j | (f_i, f_j) \in E^f_{\text{KNN}}\}$ to denote neighborhood of f_i.

Token-expanded Atom Graph The atom graph is constructed through expanding each token-level edge from E^f_{KNN} into several atom-level edges. More specifically, for a token-level edge in $(f_i, f_j) \in E^f_{\text{KNN}}$, we connect each atom with atoms from the other token. In practice, to control the number of atom-level edges, for an atom a_i, we connect $a_s \in f_i$ with the k-nearest atoms in f_j. Through this expansion, we obtain a set of atom-level edges that contain short-range interactions within atoms' neighborhoods, as well as long-range interactions bridged by token-level edges. Finally, we get the set of atom-level edges $E^a_{\text{knn}} = \{(a_s, a_t) | a_s \in f_i, a_t \in \text{knn}(f_j, a_s), (f_i, f_j) \in E^f_{\text{KNN}}\}$, and we use $\text{knn}(f_i, f_j)$ to denote the set of atom-level edges expanded from (f_i, f_j).

3.2.3 Bilevel Message Passing

Prepared with aforementioned atom embeddings $[H_p^0; H_l^0]$ and token-grouped atom-level edges E^a_{knn}, we now introduce our bilevel message passing through equivariant bilevel graph attention.

Equivariant Bilevel Graph Attention For a token edge $(f_i, f_j) \in E^f_{\text{KNN}}$ and their expanded atom edges $\{(a_s, a_t)|a_s \in f_i, a_t \in \text{knn}(f_j, a_s)\}$, we first compute *atom-level cross attention* based on input atom embeddings H^{l-1}, where l is the current layer:

$$[\mathbf{Q}^l; \mathbf{K}^l; \mathbf{V}^l] = \text{Linear}(H^{l-1}), \tag{6}$$

$$\text{Score} : S_{i,j}[a_s, a_t] = \text{MLP}(\mathbf{Q}^l[a_s], \mathbf{K}^l[a_t], \text{RBF}(D[a_s, a_t]), \mathbf{e}_{i,j}), \tag{7}$$

$$\text{Attention Weight} : \alpha_{i,j}[a_s, a_t] = \text{Softmax}_{a_t \in \text{knn}(f_j, a_s)}(S_{i,j}[a_s, a_t]W_\alpha), \tag{8}$$

where $\mathbf{Q}^l[a_s], \mathbf{K}^l[a_t]$ are query and key vectors of a_s, a_t, $\text{RBF}(D[a_s, a_t])$ embeds the relative position of a_t to a_s, $\mathbf{e}_{i,j}$ is the edge type embedding of (f_i, f_j)[6], and W_α is to project the scores into scalars. Through Softmax in Eq. 8, a_s is able to aggregate messages from $a_t \in \text{knn}(f_j, a_s)$, namely .

The *token-level cross attention* is defined through aggregating all atom-level edges expanded from the token-level edge.

$$\text{Score} : S_{i,j} = \frac{1}{|\text{knn}(f_i, f_j)|} \sum_{(a_s, a_t) \in \text{knn}(f_i, f_j)} M_{i,j}[a_s, a_t], \tag{9}$$

$$\text{Attention Weight} : \beta_{i,j} = \text{Softmax}_{f_j \in \text{KNN}(f_i)}(S_{i,j}W_\beta), \tag{10}$$

where W_β projects the scores into scalars. Basically, $S_{i,j}$ aggregates all atom-level edges expanded from (f_i, f_j). Then we have the following message passing and embedding update:

$$\mathbf{m}_{i,j}[a_s] = \sum_{a_t \in \text{knn}(f_j, a_s)} \alpha_{i,j}[a_s, a_t]\mathbf{V}^l[a_t], \tag{11}$$

$$\mathbf{m}_i[a_s] = \sum_{f_j \in \text{KNN}(f_i)} \beta_{i,j}\text{MLP}(\mathbf{m}_{i,j}[a_s]), \tag{12}$$

$$H^l[a_s] \leftarrow H^{l-1}[a_s] + \text{ScatterMean}(\mathbf{m}_i[a_s], \mathcal{T}_{f2a}). \tag{13}$$

where $\mathbf{V}^l[a_t]$ is the value vector of a_t at layer-l. Stacking equivariant bilevel attention, equivariant feed-forward layer, and equivariant layer normalization together, we obtain an equivariant graph Transformer layer, as shown in Figure 2 C. For more details, please refer to Appendix A.2.

4 Experiments and Results

In this section, we evaluate our OverlapBPE and h-MINT model in two fundamental drug discovery tasks: binding affinity prediction (Section 4.1) and virtual screening (Section 4.2). We conduct further experiments and case study for OverlapBPE in incorporating chemical information and representing chirality in Section 4.3.

4.1 Binding Affinity Prediction

Task Definition Given the 3D structure of a pocket-ligand pair, the task is to predict the binding affinity, *i.e.*, change in free energy upon binding. The input is a complex (p, l) with 3D structure, and the output is a real value y. Performance is assessed with regression metrics such as root-mean-square error (RMSE) and Pearson/Spearman correlation against experimental affinities.

Setup We follow Somnath et al. (2021); Wang et al. to conduct experiments on the well-established **PDBBind** benchmark (Wang et al., 2005) and split the 4,709 complexes according to sequence identity of the protein using a 30% threshold. We also employ the **LBA** dataset with its predefined splits from the Atom3D benchmark (Townshend et al., 2020), comprising 3,507 protein-ligand complexes for training, 466 for validation, and 490 for testing. For the baseline models, we compare against a variety of approaches (Öztürk et al., 2018; Bepler & Berger, 2019; Rao et al., 2019; Elnaggar et al., 2022; Gainza et al., 2020; Hermosilla et al., 2020; Somnath et al., 2021; Wang et al., 2022; Jing et al., 2021; Townshend et al., 2020; Schütt et al., 2017; Gasteiger et al., 2021; Zhou et al., 2023; Gao et al.; Feng et al.). Details are provided in Appendix B.1. Among these models, we primarily focus our comparison on GET (Kong et al., 2024) and its variants, as it currently achieves the best performance

[6]We use different edge types to distinguish intra- and inter-molecule edges.

Table 1: **Mean and standard deviation of three runs on the PDBBind benchmark**. The best results are marked in **bold**, and the second best are underlined. Baseline results are borrowed from (Wang et al.; Kong et al., 2024). Details in Appendix B.

	Model	RMSE ↓	Pearson ↑	Spearman ↑
Separate Encoder	DeepDTA	1.866 ± 0.080	0.472 ± 0.022	0.471 ± 0.024
	Bepler and Berger's	1.985 ± 0.006	0.165 ± 0.006	0.152 ± 0.024
	TAPE	1.890 ± 0.035	0.338 ± 0.044	0.286 ± 0.124
	ProtTrans	1.544 ± 0.015	0.438 ± 0.053	0.434 ± 0.058
	MaSIF	1.484 ± 0.018	0.467 ± 0.020	0.455 ± 0.014
	IEConv	1.554 ± 0.016	0.414 ± 0.053	0.428 ± 0.032
	Holoprot-Full Surface	1.464 ± 0.006	0.509 ± 0.002	0.500 ± 0.005
	Holoprot-Superpixel	1.491 ± 0.004	0.491 ± 0.014	0.482 ± 0.032
	ProNet-Amino Acid	1.455 ± 0.009	0.536 ± 0.012	0.526 ± 0.012
	ProNet-Backbone	1.458 ± 0.003	0.546 ± 0.007	0.550 ± 0.008
	ProNet-All-Atom	1.463 ± 0.001	0.551 ± 0.005	0.551 ± 0.008
	ESM-2 + fingerprint	1.537 ± 0.001	0.455 ± 0.013	0.433 ± 0.009
Joint Encoder	GVP	1.594 ± 0.073	-	-
	Atom3D-3DCNN	1.416 ± 0.021	0.550 ± 0.021	0.553 ± 0.009
	Atom3D-ENN	1.568 ± 0.012	0.389 ± 0.024	0.408 ± 0.021
	Atom3D-GNN	1.601 ± 0.048	0.545 ± 0.027	0.533 ± 0.033
	GET	1.430 ± 0.007	0.586 ± 0.001	0.575 ± 0.002
	GET-Murcko	1.415 ± 0.010	0.590 ± 0.002	0.578 ± 0.003
	GET-BRICS	1.410 ± 0.008	0.592 ± 0.003	0.579 ± 0.004
	GET-PS	1.387 ± 0.015	0.601 ± 0.002	0.582 ± 0.005
	Ours	**1.295 ± 0.001**	**0.640 ± 0.002**	**0.625 ± 0.002**

and shares similarity with our method. Specifically, we include *GET-PS*, *GET-Murcko*, and *GET-BRICS*, which are GET models incorporating the Principal Subgraph tokenization (Kong et al., 2022b), Bemis-Murcko scaffolding (Bemis & Murcko, 1996), and BRICS tokenization (Wegscheid-Gerlach et al.). We also include another baseline (ESM-2+fingerprint) which incorporates ESM-2 embedding to represents pockets and traditional fingerprints (Morgan+ERP+Avalon) to represent molecules.

Results We employ OverlapBPE on the ligand molecules while utilizing residues as tokens for pockets, and conduct evaluations on PDBbind and LBA datasets separately. Table 1 and 2 report the mean and the standard deviation of the metrics across 3 runs for the PDBbind and LBA datasets. Our model demonstrates significantly better performance over baseline methods in the binding affinity prediction task. Our improvement suggests that our tokenization and modeling may better preserve interaction-relevant chemical features. Significance test and more detailed analysis are in Appendix B.

4.2 Structure-based Virtual Screening

Task Definition Given the 3D structure of a pocket p and a library of ligands $\{l_i\}$, the task is to retrieve candidate ligands that are possible to bind with p. A Virtual Screening (VS) model learns a score s_i for each pair (p, l_i), and ranks all candidate ligands in descending order of s_i. The evaluation metrics include the area under the ROC curve (AUC), enrichment factor at a given top-k threshold (EF@k), and BEDROC, which emphasize early-recognition of true binders.

Setup Evaluation was performed on DUD-E (Mysinger et al., 2012) (102 targets, 22,886 actives) following preprocessing by Gao et al. (2023), and additionally on LIT-PCBA (Tran-Nguyen et al., 2020), DEKOIS (Vogel et al., 2011), and JACS/Merck (Wang et al., 2015; Schindler et al., 2020) as used in (Feng et al., 2025) (results in Appendix C.4). We benchmark against classical docking tools (Halgren et al., 2004; Trott et al., 2009), early ML scoring functions (Durrant & Mccammon, 2011; Ballester et al., 2010; Stepniewska-Dziubinska et al., 2017; Zheng et al., 2019; Zhang et al., 2023), and contrastive learning frameworks DrugCLIP (Gao et al., 2023) and LigUnity (Feng et al., 2025). Since DrugCLIP and LigUnity use different training sets, for a fair comparison, we train these models and our model with PDBBind (Wang et al., 2005) only, which comprises 16,744 pocket-ligand pairs, with any overlap with the test sets removed. Following the conventions (Feng et al., 2025; Gao et al., 2023), these models are initialized with pretrained checkpoint of UniMol (Zhou et al., 2023), with loss definitions and further implementation details in Appendix C.

Table 2: **Mean and standard deviation of three runs on LBA prediction**. The baseline results are from Kong et al. (2024). Models with * are large pretrained models, results from (Gao et al.; Feng et al.). The best results are marked in **bold** and the second best are underlined. *Note:* To save space, we only report the best baseline settings from atom-level, fragment-level, and bi-level. Details in Appendix B.

Best Repr. Setting	Model	RMSE ↓	Pearson ↑	Spearman ↑
Atom-level	SchNet	1.357 ± 0.017	0.598 ± 0.011	0.592 ± 0.015
	EGNN	1.358 ± 0.000	0.599 ± 0.002	0.587 ± 0.004
	LEFTNet	1.343 ± 0.004	0.610 ± 0.004	0.598 ± 0.003
	ET	1.367 ± 0.037	0.599 ± 0.017	0.584 ± 0.025
	UniMol*	1.434	0.565	0.540
	BigBind*	1.340	0.632	0.620
	ProFSA*	1.377	0.628	0.620
Frag-level	GemNet	1.393 ± 0.036	0.569 ± 0.027	0.553 ± 0.026
	Equiformer	1.350 ± 0.019	0.604 ± 0.013	0.591 ± 0.012
	DimeNet++	1.388 ± 0.010	0.582 ± 0.009	0.574 ± 0.007
Bi-level	MACE	1.372 ± 0.021	0.612 ± 0.010	0.592 ± 0.010
	GET	1.331 ± 0.008	0.618 ± 0.005	0.607 ± 0.005
	GET-PS	1.312 ± 0.016	0.631 ± 0.011	0.642 ± 0.011
	Ours	**1.276 ± 0.011**	**0.660 ± 0.001**	**0.661 ± 0.001**

Table 3: **Zero-shot Virtual Screening on DUD-E**. Baseline results are from (Gao et al., 2023; Feng et al., 2025). Models with * are trained with PDBBind data only for fair comparison. Details in Appendix C.

	AUC (%) ↑	BEDROC (%) ↑	EF ↑ 0.5%	EF ↑ 1%	EF ↑ 5%
Glide-SP	76.70	40.70	19.39	16.18	7.23
Vina	71.60	-	9.13	7.32	4.44
NN-score	68.30	12.20	4.16	4.02	3.12
RFscore	65.21	12.41	4.90	4.52	2.98
Pafnucy	63.11	16.50	4.24	3.86	3.76
OnionNet	59.71	8.62	2.84	2.84	2.20
Planet	71.60	-	10.23	8.83	5.40
DrugCLIP *	81.39	45.96	34.27	29.01	10.18
LigUnity *	81.69	46.01	34.44	29.07	10.26
Ours *	**84.45**	**47.64**	**35.06**	**29.91**	**10.76**

Results As shown in Table 3, our model successfully generalizes to the DUD-E benchmark under the zero-shot setting, thanks to the expressiveness of the proposed OverlapBPE and the supporting model h-MINT. Notably, our method surpasses the state-of-the-art baselines in terms of all the metrics, indicating its strong ability of capturing precise protein-ligand interaction patterns.

4.3 Additional Analysis of Tokenization

In this section, we provide additional analysis about our tokenization method's advantages in two aspects: incorporating chemical information and representing chirality.

Incorporating chemical information. Figure 3 illustrates a case study from the LBA dataset. Our tokenization preserves the integrity of the benzene ring and retains the positive charge of `[N+]`, which is necessary for forming the pi-cation interaction between the ligand and the protein pocket. In contrast, the PS tokenization treats `[N]` as neutral and thus cannot capture this interaction. This difference contributes to more accurate affinity prediction, with our method achieving an error of 0.56 compared to 0.67 for the PS tokenization.

Representing chirality. To further validate the effectiveness of our overlap tokenization and its capability to represent chirality, we followed MolKGNN (Liu et al., 2023) and conducted high-throughput screening (HTS) experiments on PubChem assays as a binary classification task. Specifically, we only use the OverlapBPE tokenization with XGBoost (Chen & Guestrin, 2016) and do not adopt the

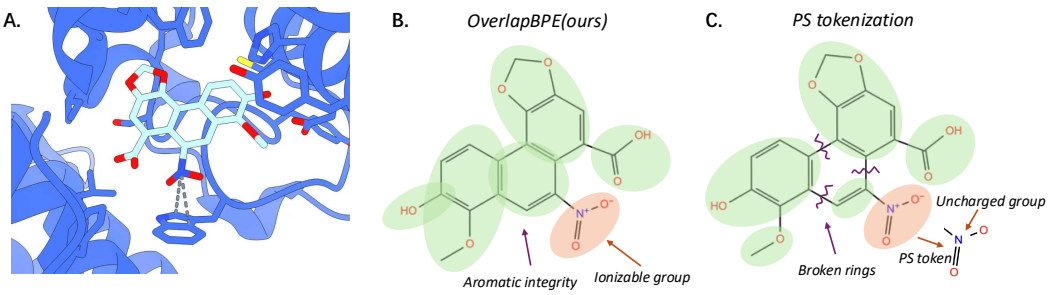

Figure 3: **OverlapBPE (ours) better preserves aromatic bond integrity, and ionic state**. (A) An interaction formed between the ligand and the protein pocket. The ligand contains a positively charged `[N+]`, which forms two π-cation interactions with two aromatic rings in the protein pocket. (B) Representation using our tokenization method. Green colors indicate fragments without charge. Red colors indicate charged fragments. (C) Representation using the PS tokenization method, where green and red indicate fragments as above, but the `[N+]` charge is not preserved, and some rings are broken.

h-MINT model for two reasons: (i) the dataset lacks target structures, and (ii) HTS places stringent demands on efficiency. We evaluate OverlapBPE on 8 PubChem HTS assays in Table 4. The baselines include strong atom-level GNN models such as SchNet (Schütt et al., 2017), SphereNet (Liu et al., 2022), ChiRo (Adams et al., 2021), KerGNNs (Feng et al., 2022) and MolKGNN (Liu et al., 2023). For OverlapBPE, we investigate two variants: a *chiral* vocabulary that preserves chirality in tokens, and a *non-chiral* vocabulary that omits stereochemical information. All baselines rely on extensive molecular features and complex model architectures, whereas our method only utilizes tokenized bag-of-words features combined with XGBoost for classification. We report early-enrichment performance using $\text{logAUC}_{[0.001,0.1]}$ in Table 4 and can observe that: (i) Our chiral method significantly outperforms non-chiral one, showing the importance of chirality information in HTS tasks; (ii) Our method outperforms all baselines in average ranking, and even exceeds ChiRo and MolKGNN, which are designed to represent molecular chirality; (iii) Leveraging XGBoost's lightweight feature, our method completes training and prediction within 1 second.

Table 4: **Early-enrichment performance on PubChem HTS assays**. Metric is $\text{logAUC}_{[0.001,0.1]}$ (higher is better). **Ours (chiral)** preserves the chirality of tokens and **Ours (non-chiral)** does not. Bold numbers indicate the best method per dataset. Baseline results are taken from Liu et al. (2023).

PubChem AID	MolKGNN	SchNet	SphereNet	DimeNet++	ChiRo	KerGNN	Ours (chiral)	Ours (non-chiral)
435008	**0.255**	0.187	0.215	0.203	0.168	0.147	0.221	0.211
1798	0.174	0.195	0.196	0.208	0.165	0.078	0.217	**0.282**
435034	0.227	0.246	0.230	0.235	0.211	0.179	**0.281**	0.261
2258	0.301	0.240	**0.380**	0.340	0.251	0.195	0.265	0.246
463087	0.390	0.332	**0.399**	0.389	0.258	0.150	0.338	0.322
488997	0.303	0.319	0.309	0.315	0.193	0.081	**0.384**	0.376
2689	**0.415**	0.324	0.401	0.367	0.351	0.264	0.348	0.343
485290	**0.498**	0.333	0.450	0.463	0.295	0.223	0.474	0.341
Avg. Rank	3.250	5.250	3.125	3.375	6.375	8.000	**2.625**	4.000

5 Discussion and Future Work

We introduced OverlapBPE and h-MINT, an efficient tokenization-plus-learning framework for protein–ligand interactions that achieves superior performance on virtual screening and affinity prediction. For future work, we would like to explore ways to incorporate other domain knowledge (*e.g.*, PAINS) that is infrequent but crucial for drug discovery. Besides, we plan to extend h-MINT to docking pose prediction and broader structure-based drug design.

Ethics Statement

Small-molecule modeling plays a critical role in drug discovery, with broad potential applications in therapeutic development, virtual screening, and rational design of ligands targeting protein pockets. Advances in representation learning and interaction modeling offer new opportunities to accelerate discovery and improve our understanding of molecular interactions, which may positively impact medicine, biotechnology, and related fields.

At the same time, we recognize that such computational approaches also carry potential risks, particularly regarding misuse in unsafe or unethical drug design. To mitigate these risks, this study is conducted exclusively on publicly available datasets and strictly follows established ethical guidelines. We advocate for the responsible research and application of molecular modeling methods to ensure their development contributes to societal benefit.

Reproducibility Statement

We ensure that the training data, training and inference procedures, and result evaluations are all reproducible. The appendix provides all necessary details and offers a comprehensive explanation of each component of this work. The datasets used are publicly available, and the model implementation is based on the open-source GET (Kong et al., 2024), LigUnity (Feng et al., 2025) and MolKGNN (Liu et al., 2023) codebases. The code and models used for evaluation are also publicly accessible and cited in the appendix. Furthermore, we describe the training hyperparameters in detail in the appendix, thereby ensuring that the entire experimental process is fully reproducible.

References

Keir Adams, Lagnajit Pattanaik, and Connor W Coley. Learning 3d representations of molecular chirality with invariance to bond rotations. *arXiv preprint arXiv:2110.04383*, 2021.

Namrata Anand and Tudor Achim. Protein structure and sequence generation with equivariant denoising diffusion probabilistic models. *arXiv preprint arXiv:2205.15019*, 2022.

Kenneth Atz, Francesca Grisoni, and Gisbert Schneider. Geometric deep learning on molecular representations. *Nature Machine Intelligence*, 3(12):1023–1032, 2021.

Ballester, P., J., Mitchell, J., and B. A machine learning approach to predicting protein-ligand binding affinity with applications to molecular docking. *Bioinformatics Oxford*, 2010.

Ilyes Batatia, David P Kovacs, Gregor Simm, Christoph Ortner, and Gábor Csányi. Mace: Higher order equivariant message passing neural networks for fast and accurate force fields. *Advances in Neural Information Processing Systems*, 35:11423–11436, 2022.

Guy W Bemis and Mark A Murcko. The properties of known drugs. 1. molecular frameworks. *Journal of medicinal chemistry*, 39(15):2887–2893, 1996.

Tristan Bepler and Bonnie Berger. Learning protein sequence embeddings using information from structure. *arXiv preprint arXiv:1902.08661*, 2019.

Tianqi Chen and Carlos Guestrin. Xgboost: A scalable tree boosting system. In *Proceedings of the 22nd acm sigkdd international conference on knowledge discovery and data mining*, pp. 785–794, 2016.

Weitao Du, Yuanqi Du, Limei Wang, Dieqiao Feng, Guifeng Wang, Shuiwang Ji, Carla Gomes, and Zhi-Ming Ma. A new perspective on building efficient and expressive 3d equivariant graph neural networks. *arXiv preprint arXiv:2304.04757*, 2023.

J. D. Durrant and J. A. Mccammon. Nnscore 2.0: A neural-network receptor–ligand scoring function. *Journal of Chemical Information & Modeling*, 51(11):2897, 2011.

Ahmed Elnaggar, Michael Heinzinger, Christian Dallago, Ghalia Rehawi, Yu Wang, Llion Jones, Tom Gibbs, Tamas Feher, Christoph Angerer, Martin Steinegger, Debsindhu Bhowmik, and Burkhard Rost. Prottrans: Toward understanding the language of life through self-supervised learning. *IEEE Transactions on Pattern Analysis and Machine Intelligence*, 44(10):7112–7127, 2022. doi: 10.1109/TPAMI.2021.3095381.

Aosong Feng, Chenyu You, Shiqiang Wang, and Leandros Tassiulas. Kergnns: Interpretable graph neural networks with graph kernels. In *Proceedings of the AAAI conference on artificial intelligence*, volume 36, pp. 6614–6622, 2022.

Bin Feng, Zijing Liu, Mingjun Yang, Junjie Zou, He Cao, Yu Li, Lei Zhang, and Sheng Wang. A foundation model for protein-ligand affinity prediction through jointly optimizing virtual screening and hit-to-lead optimization. *bioRxiv*, pp. 2025–02, 2025.

Shikun Feng, Minghao Li, Yinjun Jia, Wei-Ying Ma, and Yanyan Lan. Protein-ligand binding representation learning from fine-grained interactions. In *The Twelfth International Conference on Learning Representations*.

Pablo Gainza, Freyr Sverrisson, Frederico Monti, Emanuele Rodola, D Boscaini, MM Bronstein, and BE Correia. Deciphering interaction fingerprints from protein molecular surfaces using geometric deep learning. *Nature Methods*, 17(2):184–192, 2020.

Bowen Gao, Yinjun Jia, YuanLe Mo, Yuyan Ni, Wei-Ying Ma, Zhi-Ming Ma, and Yanyan Lan. Self-supervised pocket pretraining via protein fragment-surroundings alignment. In *The Twelfth International Conference on Learning Representations*.

Bowen Gao, Bo Qiang, Haichuan Tan, Yinjun Jia, Minsi Ren, Minsi Lu, Jingjing Liu, Wei-Ying Ma, and Yanyan Lan. Drugclip: Contrastive protein-molecule representation learning for virtual screening. *Advances in Neural Information Processing Systems*, 36:44595–44614, 2023.

Zhangyang Gao, Cheng Tan, Pablo Chacón, and Stan Z Li. Pifold: Toward effective and efficient protein inverse folding. *arXiv preprint arXiv:2209.12643*, 2022.

Johannes Gasteiger, Shankari Giri, Johannes T Margraf, and Stephan Günnemann. Fast and uncertainty-aware directional message passing for non-equilibrium molecules. *arXiv preprint arXiv:2011.14115*, 2020.

Johannes Gasteiger, Florian Becker, and Stephan Günnemann. Gemnet: Universal directional graph neural networks for molecules. *Advances in Neural Information Processing Systems*, 34: 6790–6802, 2021.

Zijie Geng, Shufang Xie, Yingce Xia, Lijun Wu, Tao Qin, Jie Wang, Yongdong Zhang, Feng Wu, and Tie-Yan Liu. De novo molecular generation via connection-aware motif mining. *arXiv preprint arXiv:2302.01129*, 2023.

Thomas A. Halgren, Robert B. Murphy, Richard A. Friesner, Hege S. Beard, Leah L. Frye, W. Thomas Pollard, and Jay L. Banks. Glide: a new approach for rapid, accurate docking and scoring. 2. enrichment factors in database screening. *Journal of Medicinal Chemistry*, 47(7):1750–1759, 2004.

Pedro Hermosilla, Marco Schäfer, Matěj Lang, Gloria Fackelmann, Pere Pau Vázquez, Barbora Kozlíková, Michael Krone, Tobias Ritschel, and Timo Ropinski. Intrinsic-extrinsic convolution and pooling for learning on 3d protein structures. *arXiv preprint arXiv:2007.06252*, 2020.

Emiel Hoogeboom, Vıctor Garcia Satorras, Clément Vignac, and Max Welling. Equivariant diffusion for molecule generation in 3d. In *International Conference on Machine Learning*, pp. 8867–8887. PMLR, 2022.

Akihiro Inokuchi, Takashi Washio, and Hiroshi Motoda. An apriori-based algorithm for mining frequent substructures from graph data. In *European conference on principles of data mining and knowledge discovery*, pp. 13–23. Springer, 2000.

Ali Jazayeri and Chris Yang. Frequent subgraph mining algorithms in static and temporal graph-transaction settings: A survey. *IEEE Transactions on Big Data*, 2021.

Yinjun Jia, Bowen Gao, Jiaxin Tan, Jiqing Zheng, Xin Hong, Wenyu Zhu, Haichuan Tan, Yuan Xiao, Liping Tan, Hongyi Cai, et al. Deep contrastive learning enables genome-wide virtual screening. *bioRxiv*, pp. 2024–09, 2024.

Wengong Jin, Regina Barzilay, and Tommi Jaakkola. Junction tree variational autoencoder for molecular graph generation. In *International Conference on Machine Learning*, pp. 2323–2332, 2018.

Wengong Jin, Regina Barzilay, and Tommi Jaakkola. Hierarchical generation of molecular graphs using structural motifs. In *International Conference on Machine Learning*, pp. 4839–4848. PMLR, 2020.

Wengong Jin, Regina Barzilay, and Tommi Jaakkola. Antibody-antigen docking and design via hierarchical equivariant refinement. *arXiv preprint arXiv:2207.06616*, 2022.

Bowen Jing, Stephan Eismann, Patricia Suriana, Raphael JL Townshend, and Ron Dror. Learning from protein structure with geometric vector perceptrons. *arXiv preprint arXiv:2009.01411*, 2020.

Bowen Jing, Stephan Eismann, Pratham N Soni, and Ron O Dror. Equivariant graph neural networks for 3d macromolecular structure. *arXiv preprint arXiv:2106.03843*, 2021.

Xiangzhe Kong, Wenbing Huang, and Yang Liu. Conditional antibody design as 3d equivariant graph translation. *arXiv preprint arXiv:2208.06073*, 2022a.

Xiangzhe Kong, Wenbing Huang, Zhixing Tan, and Yang Liu. Molecule generation by principal subgraph mining and assembling. *Advances in Neural Information Processing Systems*, 35: 2550–2563, 2022b.

Xiangzhe Kong, Wenbing Huang, and Yang Liu. Generalist equivariant transformer towards 3d molecular interaction learning. In *International Conference on Machine Learning*, pp. 25149–25175. PMLR, 2024.

Michihiro Kuramochi and George Karypis. Frequent subgraph discovery. In *Proceedings 2001 IEEE international conference on data mining*, pp. 313–320. IEEE, 2001.

Xinhao Li and Denis Fourches. Smiles pair encoding: a data-driven substructure tokenization algorithm for deep learning. *Journal of chemical information and modeling*, 61(4):1560–1569, 2021.

Yi-Lun Liao and Tess Smidt. Equiformer: Equivariant graph attention transformer for 3d atomistic graphs. *arXiv preprint arXiv:2206.11990*, 2022.

Yi Liu, Limei Wang, Meng Liu, Yuchao Lin, Xuan Zhang, Bora Oztekin, and Shuiwang Ji. Spherical message passing for 3d molecular graphs. In *International Conference on Learning Representations (ICLR)*, 2022.

Yunchao Lance Liu, Yu Wang, Oanh Vu, Rocco Moretti, Bobby Bodenheimer, Jens Meiler, and Tyler Derr. Interpretable chirality-aware graph neural network for quantitative structure activity relationship modeling in drug discovery. In *Proceedings of the AAAI conference on artificial intelligence*, volume 37, pp. 14356–14364, 2023.

Shitong Luo, Yufeng Su, Xingang Peng, Sheng Wang, Jian Peng, and Jianzhu Ma. Antigen-specific antibody design and optimization with diffusion-based generative models. *bioRxiv*, pp. 2022–07, 2022.

Christopher W Murray and David C Rees. The rise of fragment-based drug discovery. *Nature chemistry*, 1(3):187–192, 2009.

Michael M Mysinger, Michael Carchia, John J Irwin, and Brian K Shoichet. Directory of useful decoys, enhanced (dud-e): better ligands and decoys for better benchmarking. *Journal of medicinal chemistry*, 55(14):6582–6594, 2012.

Siegfried Nijssen and Joost N Kok. A quickstart in frequent structure mining can make a difference. In *Proceedings of the tenth ACM SIGKDD international conference on Knowledge discovery and data mining*, pp. 647–652, 2004.

Hakime Öztürk, Arzucan Özgür, and Elif Ozkirimli. Deepdta: deep drug–target binding affinity prediction. *Bioinformatics*, 34(17):i821–i829, 2018.

Alasdair T R Laurie and Richard M Jackson. Methods for the prediction of protein-ligand binding sites for structure-based drug design and virtual ligand screening. *Current Protein and Peptide Science*, 7(5):395–406, 2006.

Roshan Rao, Nicholas Bhattacharya, Neil Thomas, Yan Duan, Peter Chen, John Canny, Pieter Abbeel, and Yun Song. Evaluating protein transfer learning with tape. *Advances in neural information processing systems*, 32, 2019.

Vıctor Garcia Satorras, Emiel Hoogeboom, and Max Welling. E (n) equivariant graph neural networks. In *International conference on machine learning*, pp. 9323–9332. PMLR, 2021.

Christina EM Schindler, Hannah Baumann, Andreas Blum, Dietrich Bose, Hans-Peter Buchstaller, Lars Burgdorf, Daniel Cappel, Eugene Chekler, Paul Czodrowski, Dieter Dorsch, et al. Large-scale assessment of binding free energy calculations in active drug discovery projects. *Journal of Chemical Information and Modeling*, 60(11):5457–5474, 2020.

Kristof Schütt, Pieter-Jan Kindermans, Huziel Enoc Sauceda Felix, Stefan Chmiela, Alexandre Tkatchenko, and Klaus-Robert Müller. Schnet: A continuous-filter convolutional neural network for modeling quantum interactions. *Advances in neural information processing systems*, 30, 2017.

Kristof T Schütt, Huziel E Sauceda, P-J Kindermans, Alexandre Tkatchenko, and K-R Müller. SchNet–A deep learning architecture for molecules and materials. *The Journal of Chemical Physics*, 148(24), 2018.

Rico Sennrich, Barry Haddow, and Alexandra Birch. Neural machine translation of rare words with subword units. In *Proceedings of the 54th Annual Meeting of the Association for Computational Linguistics (Volume 1: Long Papers)*, pp. 1715–1725, 2016.

Yuchen Shen and Barnabás Póczos. Graphbpe: Molecular graphs meet byte-pair encoding. *arXiv preprint arXiv:2407.19039*, 2024.

Vignesh Ram Somnath, Charlotte Bunne, and Andreas Krause. Multi-scale representation learning on proteins. *Advances in Neural Information Processing Systems*, 34:25244–25255, 2021.

Hannes Stärk, Dominique Beaini, Gabriele Corso, Prudencio Tossou, Christian Dallago, Stephan Günnemann, and Pietro Liò. 3d infomax improves gnns for molecular property prediction. In *International Conference on Machine Learning*, pp. 20479–20502. PMLR, 2022.

Marta M. Stepniewska-Dziubinska, Piotr Zielenkiewicz, and Paweł Siedlecki. Pafnucy - a deep neural network for structure-based drug discovery. *ArXiv*, abs/1712.07042, 2017.

Philipp Thölke and Gianni De Fabritiis. Torchmd-net: equivariant transformers for neural network based molecular potentials. *arXiv preprint arXiv:2202.02541*, 2022.

Raphael JL Townshend, Martin Vögele, Patricia Suriana, Alexander Derry, Alexander Powers, Yianni Laloudakis, Sidhika Balachandar, Bowen Jing, Brandon Anderson, Stephan Eismann, et al. Atom3d: Tasks on molecules in three dimensions. *arXiv preprint arXiv:2012.04035*, 2020.

Viet-Khoa Tran-Nguyen, Célien Jacquemard, and Didier Rognan. Lit-pcba: an unbiased data set for machine learning and virtual screening. *Journal of chemical information and modeling*, 60(9): 4263–4273, 2020.

Trott, Oleg, Olson, Arthur, and J. Autodock vina: Improving the speed and accuracy of docking with a new scoring function, efficient optimization, and multithreading. *J. Comput. Chem.*, 31(2): NA–NA, 2009.

Umit V Ucak, Islambek Ashyrmamatov, and Juyong Lee. Improving the quality of chemical language model outcomes with atom-in-smiles tokenization. *Journal of cheminformatics*, 15(1):55, 2023.

Simon M Vogel, Matthias R Bauer, and Frank M Boeckler. Dekois: Demanding evaluation kits for objective in silico screening a versatile tool for benchmarking docking programs and scoring functions. *Journal of chemical information and modeling*, 51(10):2650–2665, 2011.

Limei Wang, Haoran Liu, Yi Liu, Jerry Kurtin, and Shuiwang Ji. Learning hierarchical protein representations via complete 3d graph networks. In *The Eleventh International Conference on Learning Representations*.

Limei Wang, Haoran Liu, Yi Liu, Jerry Kurtin, and Shuiwang Ji. Learning protein representations via complete 3d graph networks. *arXiv preprint arXiv:2207.12600*, 2022.

Lingle Wang, Yujie Wu, Yuqing Deng, Byungchan Kim, Levi Pierce, Goran Krilov, Dmitry Lupyan, Shaughnessy Robinson, Markus K Dahlgren, Jeremy Greenwood, et al. Accurate and reliable prediction of relative ligand binding potency in prospective drug discovery by way of a modern free-energy calculation protocol and force field. *Journal of the American Chemical Society*, 137 (7):2695–2703, 2015.

Renxiao Wang, Xueliang Fang, Yipin Lu, Chao-Yie Yang, and Shaomeng Wang. The pdbbind database: methodologies and updates. *Journal of medicinal chemistry*, 48(12):4111–4119, 2005.

Christof Wegscheid-Gerlach, Andrea Zaliani, and Matthias Rarey. On the art of compiling and using'drug-like'chemical fragment spaces.

Daniel S Wigh, Jonathan M Goodman, and Alexei A Lapkin. A review of molecular representation in the age of machine learning. *Wiley Interdisciplinary Reviews: Computational Molecular Science*, 12(5):e1603, 2022.

Minkai Xu, Lantao Yu, Yang Song, Chence Shi, Stefano Ermon, and Jian Tang. Geodiff: A geometric diffusion model for molecular conformation generation. *arXiv preprint arXiv:2203.02923*, 2022.

Xifeng Yan and Jiawei Han. gspan: Graph-based substructure pattern mining. In *2002 IEEE International Conference on Data Mining, 2002. Proceedings.*, pp. 721–724. IEEE, 2002.

Soojung Yang, Doyeong Hwang, Seul Lee, Seongok Ryu, and Sung Ju Hwang. Hit and lead discovery with explorative rl and fragment-based molecule generation. *Advances in Neural Information Processing Systems*, 34, 2021.

Sheheryar Zaidi, Michael Schaarschmidt, James Martens, Hyunjik Kim, Yee Whye Teh, Alvaro Sanchez-Gonzalez, Peter Battaglia, Razvan Pascanu, and Jonathan Godwin. Pre-training via denoising for molecular property prediction. *arXiv preprint arXiv:2206.00133*, 2022.

Xiangying Zhang, Haotian Gao, Haojie Wang, Zhihang Chen, Zhe Zhang, Xinchong Chen, Yan Li, Yifei Qi, and Renxiao Wang. Planet: A multi-objective graph neural network model for protein–ligand binding affinity prediction, 2023. URL https://doi.org/10.1101/2023.02.01.526585.

Liangzhen Zheng, Jingrong Fan, and Yuguang Mu. Onionnet: a multiple-layer intermolecular-contact-based convolutional neural network for protein–ligand binding affinity prediction. *ACS omega*, 4 (14):15956–15965, 2019.

Gengmo Zhou, Zhifeng Gao, Qiankun Ding, Hang Zheng, Hongteng Xu, Zhewei Wei, Linfeng Zhang, and Guolin Ke. Uni-mol: A universal 3d molecular representation learning framework. In *The Eleventh International Conference on Learning Representations*, 2023. URL https://openreview.net/forum?id=6K2RM6wVqKu.

A METHOD

A.1 OVERLAPBPE

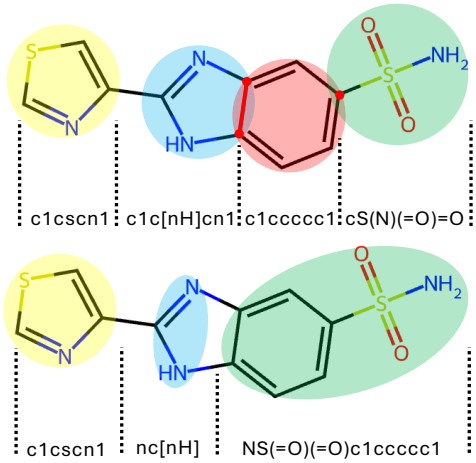

Figure 4: **Comparison of overlap (top) and non-overlap tokenization (bottom).**

Overlap vs. Non-overlap Tokenization In Figure 4, we show an example molecule tokenized in 2 different ways. We use different colors to highlight the tokenized fragments. From the top figure, we can see the molecule has 4 tokens, with 3 of the tokens sharing atoms with other tokens (we also highlight the shared atoms and bonds in red). From the bottom figure, we can see that an aromatic bond is broken and forms 2 disjoint tokens. From this figure, we can identify the difference between overlap-tokenization and non-overlap-tokenization. With overlap-tokenization better preserving the local chemical environment and better respecting the fuzzy boundaries of substructures in small molecules, we believe our novel OverlapBPE is potent to boost small molecular representation, interaction, and even generation tasks.

Example Input Here we show some example inputs to the encoder, more specifically, the embedding layer. The embedding layer takes 3 inputs: atom sequences, atom-level position codes, and token sequences, for pairs of pocket-ligands.

$$[V_p^a; V_l^a] : \texttt{[<g\_atom>, N, C, C, O, C, ..., <g\_atom>, C, C, ...]} \tag{14}$$

$$[\mathrm{Pos}(V_p^a); \mathrm{Pos}(V_l^a)] : \texttt{[<g\_pos>, `', A, `', `', B, ..., <g\_pos>, sm, sm, ...]} \tag{15}$$

$$[V_p^f; V_l^f] : \texttt{[<g\_frag>, ALA, ..., <g\_frag>, c1cscn1, ...]} \tag{16}$$

Position Code Certain types of molecules have conventional position codes to distinguish different atoms with the same element type in the same fragment, *e.g.*, `CA` and `CB` in residues. For small molecules, since there are no such conventional position codes, we simply use `sm` as the position code for all atoms in small molecules. In addition, we also add some special position codes for special tokens, e.g., `<global>`, `<mask>`, `<pad>`.

Tokenization Overhead Compared to the PS tokenizer and GET, the computational overhead of OverlapBPE and h-MINT mainly stems from the repeated calculation of atoms. We performed tokenization using OverlapBPE and PS on the 3,507 molecules in the LBA training set, and the results are shown in Table 5.

For tokenization, the number of atoms processed by OverlapBPE is 1.32 times that of PS:(7.95 × 4.5) / (8 × 3.39) = 1.32. However, since tokenization can be **executed offline and is fully parallelizable**,

Table 5: Comparison of tokenization statistics.

Tokenizer	Avg # tokens / mol	Avg # atoms / token
OverlapBPE	7.95	4.5
Principal Subgraph	8	3.39

the overhead is negligible in practice. For instance, OverlapBPE only takes **7 minutes** to process **47.9k molecules** using 32 CPUs for virtual screening training data.

A.2 H-MINT

SE-(3) Equivariance In this section, we provide more details about the model design. At first, h-MINT follows GET's (Kong et al., 2024) architecture with 2-channel updates: One is the equivariant channel, which mainly encodes and predict the coordinates of molecules following SE-(3) symmetry. The other is the invariant channel, which mainly encodes and predicts embeddings (*i.e.*, H). Thus, in general, our model is an SE-(3) equivariant model. Since we only use the embedding channel in this paper, we mainly show the update and message passing for the invariant channel. However, our model can also be extended to SE-(3) scenarios like structure prediction and generation.

Difference with GET We want to emphasize the difference between h-MINT and GET. GET is designed for non-overlap tokenization, while h-MINT is designed for overlap tokenization, and this induces a fundamental difference in model design. For GET, atoms and tokens are in a 1-1 mapping, making its model design simple and straightforward. For h-MINT, atoms and tokens are in a many-to-many mapping, which requires a bidirectional indexing system to convert atom-level embeddings to token-level embeddings and vice versa.

In Section 3.2, we present the embedding layer, graph construction, and Bilevel Graph Attention Layer. For the next, we complement other modules, including Bidirectional Equivariant Feed-Forward Network (FFN) and Bidirectional Equivariant Layer Normalization (LN).

Bidirectional Equivariant FFN For this module, the input contains the atom-level embedding H^l passed from the former module, and also the bidirectional mapping between atoms and tokens $\mathcal{T}_{a2f}, \mathcal{T}_{f2a}$. The update is as follows:

$$H^{l,f} = \text{ScatterMean}(H^l, \mathcal{T}_{a2f}) \tag{17}$$

$$H^{l'} = \text{ScatterMean}(H^{l,f}, \mathcal{T}_{f2a}) \tag{18}$$

$$H^l \leftarrow H^l + \text{MLP}([H^l; H^{l'}; \text{RBF}(D)]), \tag{19}$$

where $H^{l'}$ can be regarded as token-enhanced atom representation, and D stores the pairwise atom distances.

Bidirectional Equivariant LN This module involves normalization within each input pair, since we do not use the equivariant channel. Here, we apply simple Layer Normalization to the representations.

$$H^l \leftarrow \frac{H^l - \mathcal{E}[H^l]}{\sqrt{\text{Var}[H^l] + \epsilon}} \cdot \boldsymbol{\sigma} + \boldsymbol{\mu}, \tag{20}$$

where $\boldsymbol{\sigma}$ and $\boldsymbol{\mu}$ are learnable parameters, and $\mathcal{E}[]$ and $\text{Var}[]$ are used to calculate the mean and variance of the variable.

B Experiments: Binding Affinity Prediction

B.1 PDBBind Benchmark

We follow the data processing of (Somnath et al., 2021; Wang et al.) to conduct experiments on the PDBBind (v2019) Benchmark. More specifically, we use the split with a sequence identity of 30% to prevent leakage. This filtering results in 4,709 complexes, which are then split into 3,507,

466, and 490 for training, validation, and testing (Somnath et al., 2021). We directly borrow the baseline results from (Wang et al.; Kong et al., 2024). The main advantage of GET-PS and our model is tokenizing small molecules into fragments. To evaluate these models, we simply remove pairs without small molecules, which results in a slightly smaller split (4436 samples) compared to the original identity30 data split (4463 samples).

B.2 Implementation Details

We conduct experiments on 1 RTX A6000 GPU. Each model is trained with the Adam optimizer and learning rate decay. Considering the number of tokens and atoms may vary with different input complexes, to safely and efficiently utilize the GPU memory, we implement a dynamic batch to include as many complexes as possible while not exceeding some threshold max_n_vertex. For graph construction, we use $k = 9$ for the KNN token graph, which means each token is connected with 9 nearest tokens within a complex. And we use $k = 3$ for the token-expanded atom graph, which means for atom $a_s \in f_i$, for each KNN of the token, $f_j \in \text{KNN}(f_i)$, a_s will connect to 3 nearest atoms in f_j. We set the RBF kernel size to be 32. For baseline models, we follow the official parameter configuration. For our model, we mainly tune the learning rate (lr $\in [1e-3, 1e-4]$), final learning rate (flr $\in [1e-3, 1e-6]$), and max number of epochs (max_epoch $\in [10, 40]$). Here we list the key hyperparameters for reproducing our results on PDBBind (lr $= 1e-4$, flr $= 1e-4$, max_epoch $= 40$) and LBA (lr $= 1e-3$, flr $= 1e-4$, max_epoch $= 20$).

B.3 Baseline Models

We include many baseline models in this section of experiments. Here we briefly introduce their methods. For the **PDBBind** benchmark, DeepDTA (Öztürk et al., 2018), Bepler and Berger's (Bepler & Berger, 2019), TAPE (Rao et al., 2019), ProtTrans (Elnaggar et al., 2022), MaSIF Gainza et al. (2020), IEConv (Hermosilla et al., 2020), Holoprot (Somnath et al., 2021), and ProNet (Wang et al.) use separate encoders for pockets and ligands. GVP (Jing et al., 2020), Atom3D (Townshend et al., 2020), and GET (Kong et al., 2024) instead use a joint encoder for pockets and ligands. Inspired by the good performance and trends in joint encoder models, we also adopt a joint encoder architecture.

For the **LBA** dataset, SchNet (Schütt et al., 2018), DimeNet++ (Gasteiger et al., 2020), GemNet (Gasteiger et al., 2021) are invariant models based on invariant geometric features (*i.e.*, distance and angle). EGNN (Satorras et al., 2021), TorchMD-Net (ET) (Thölke & De Fabritiis, 2022), and LEFTNet (Du et al., 2023) preserve equivariant features and are directly implemented on 3D coordinates. MACE (Batatia et al., 2022) and Equiformer (Liao & Smidt, 2022) utilize harmonic and irreducible representations to preserve high-order equivariant features. We also include atom-level pretrained models, UniMol (Zhou et al., 2023), ProFSA (Gao et al.) and BigBind (Feng et al.). In general, all these models mainly use their invariant channel for affinity prediction, similar to GET (Kong et al., 2024) and our model; thus, we can ignore how these models deal with equivariant features in these experiments. We borrow the baseline results mainly from GET (Kong et al., 2024), which provides a complete comparison of all the above models in 3 representation settings: atom-level, fragment-level, and bi-level. To save space, we include each model's best representation setting only.

B.4 Additional Experiment Analysis

Significance of Improvements Since the benchmarks (PDBBind and LBA) are relatively small, to guarantee fair comparison and consistent results, we report mean and std for 3 runs in Table 1 and 2. Besides, we also conduct a significance test on the prediction results of GET, GET-PS and our model. And the results show p-values < 0.005 for these models in both PDBBind and LBA tasks. These evidences conclude that our model performs significantly better than the strong baselines, GET, and GET-PS.

PDBBind Results Analysis From Table 1, we can mainly draw the following conclusions: (i) Joint encoder is generally better than separate encoders. (ii) GET outperforms other baselines by a wide margin due to its hierarchical modeling, and GET-PS performs even better for better alignment between residues and small molecule fragments. (iii) Our model consistently outperforms GET and GET-PS by a wide margin (4%-5% Pearson Correlation, and 5% Spearman Correlation). We are

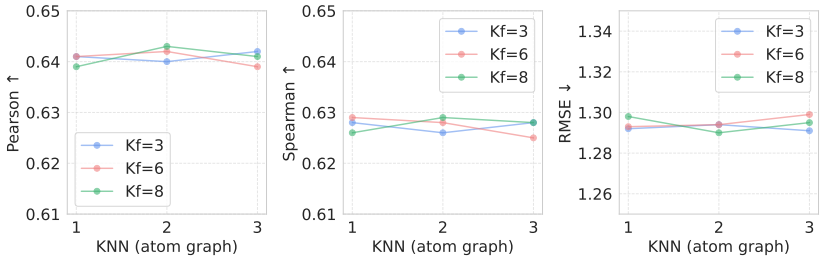

Figure 5: **Parameter study of KNN graph construction**. Kf: KNN in fragment-level graph.

also surprised by the improvements, and we recognize that the improvements come from our new tokenization, OverlapBPE, and our new model h-MINT.

As defined in Section 3.2.2, we employ K-Nearest Neighbors (KNN) to construct both fragment-level and atom-level graphs, where the choice of the hyperparameter K plays a critical role in determining the quality of graph connectivity and the overall model performance. To assess the impact of different K values, we conducted a parameter study on the PDBBind dataset. The results are illustrated in Figure 5. From the results we can see that our model is not sensitive to the choice of K. Therefore, selecting the parameter within a proper range can consistently yield satisfactory performance.

LBA Results Analysis Table 2 compares different models with atom-level, fragment-level, and bi-level representations. We borrow the baseline results from (Kong et al., 2024), which compares all baselines in all 3 representation settings. In this paper, we only include the baseline results in their best representation settings for saving space. From this table, we can see: (i) In general, bi-level representation is better than atom-level or fragment-level. This is reasonable because some molecular interactions happen on atoms (H-bond) and some happen on fragments (π stacking). Thus, we believe integrating bi-level information is crucial for modeling molecular interactions. (ii) GET and GET-PS still outperform other baselines by a wide margin (2% Pearson and Spearman Correlation), which demonstrates the effectiveness of their unified representations and model design. (iii) Last, our model outperforms GET and GET-PS even more than their improvements (3% Pearson Correlation, 2% Spearman Correlation). This result again validates the effectiveness of our OverlapBPE tokenization and our new model for many-to-many mapping between atoms and tokens.

C Experiments: Virtual Screening

C.1 Details on Loss Function

According to LigUnity (Feng et al., 2025), we optimise a composite objective

$$\mathcal{L} = \underbrace{\big(\mathcal{L}_{p\to l} + \mathcal{L}_{l\to p}\big) + \mathcal{L}_{\text{rank}}}_{\mathcal{L}_{\text{LigUnity}}} + \lambda_{\text{mse}}\mathcal{L}_{\text{mse}}, \tag{1}$$

which extends the original loss with an additional regression term.

Contrastive retrieval losses. For a mini-batch of B pocket embeddings p_i and ligand embeddings l_j we define

$$\mathcal{L}_{p\to l} = -\frac{1}{B}\sum_{i=1}^{B}\log\frac{\exp\big(\tau\,\langle p_i, l_i\rangle\big)}{\sum_{j=1}^{B}\exp\big(\tau\,\langle p_i, l_j\rangle\big)}, \qquad \mathcal{L}_{l\to p}\ \text{sym.}, \tag{2}$$

Listwise ranking loss. Given a pocket i with M_i ligands sorted by experimental affinity $\pi_1 \succ \ldots \succ \pi_{M_i}$,

$$\mathcal{L}_{\text{rank}} = -\sum_{k=1}^{M_i-1}\mu_k\,\log\frac{\exp\big(\tau\,\langle p_i, l_{\pi_k}\rangle\big)}{\sum_{t=k}^{M_i}\exp\big(\tau\,\langle p_i, l_{\pi_t}\rangle\big)}, \tag{3}$$

with positional weights $\mu_k = \frac{1}{\log(k+1)}$.

MSE loss. Similar to the regression loss implemented in the LigUnity paper, let $\hat{a}_{ij}$ be the predicted activity for pair (i, j) and a_{ij} the ground truth. With $\mathcal{P}$ the positive set, $\mathcal{N}$ represents a 20 % subsample of negatives, pocket-wise weakest positive $a_{\min,i}$ and safety margin δ, which was set to 2.0:

$$\mathcal{L}_{\text{mse}} = \frac{1}{|\mathcal{P}| + |\mathcal{N}|} \left(\sum_{(i,j)\in\mathcal{P}} (\hat{a}_{ij} - a_{ij})^2 + \sum_{(i,j)\in\mathcal{N}} \Big[\max\big(0, \hat{a}_{ij} - (a_{\min,i} - \delta)\big) \Big]^2 \right). \tag{4}$$

Throughout this paper, we fix the weights to $\lambda_{\text{mse}} = 2$. Empirically, the extra MSE term accelerates convergence and mitigates the overfit on the training dataset.

C.2 Evaluation Metrics

We assess model performance using the following metrics:

- **AUC-ROC (Area Under the Receiver Operating Characteristic curve):** measures the probability that a randomly chosen active compound is ranked higher than a randomly chosen inactive one. In our paper, we use AUC to denote it.
- **BEDROC (Boltzmann-Enhanced Discrimination of Receiver Operating Characteristic):** emphasizes early recognition of actives by applying an exponential weighting to the ROC curve, controlled by a tunable parameter. Following previous works, we set the parameter to 80.5.
- **Enrichment Factor (EF):** quantifies the fold-increase in actives found among the top percentile of the ranked library relative to random selection, reported here at 0.5%, 1%, and 5%.

C.3 Implementation Details

The implementation of virtual screening experiments includes two parts: training the baselines and finetuning our model. All the models were trained on 1 RTX 6000 GPU with 24 GB memory. For the baseline models, we retrained LigUnity (Feng et al., 2025) on the PDBBind dataset. To ensure a fair evaluation, we excluded all the samples that exist in any of the test datasets. We also followed their papers' original parameters. To evaluate, we averaged the weights of the last 3 model checkpoints. We finetuned our h-MINT model on the same PDBBind dataset. Namely, the training parameters were similar to LigUnity, with learning rate = $1e-4$, warmup ratio = 0.06, and the maximum number of ligands selected for each pocket was 16. However, we used 32-bit precision for training rather than the original 16-bit, changed the batch size to 96, and set the gradient clip to 10. We trained the model for 100 epochs initially, and observed that it converged at around the 25th epoch. Therefore, we trained it for 25 epochs and averaged the last 3 checkpoints for evaluation purposes.

C.4 Experiments on LIT-PCBA, DEKOIS and JACS/Merck dataset

C.4.1 LIT-PCBA Dataset

The LIT-PCBA dataset (Tran-Nguyen et al., 2020) is constructed from dose–response PubChem bioassays to mitigate the target and decoy selection biases found in other benchmarks. It comprises 15 protein targets with 7844 experimentally confirmed actives and 407381 inactive, which reflects realistic hit rates in high-throughput screening.

C.4.2 Additional Results and Significance Test

Table 6 reports AUC, BEDROC, and enrichment factors (EF) on LIT-PCBA in the zero-shot setting. Namely, as the original LigUnity was trained on another larger dataset Feng et al. (2025), we did not directly compare our method with it. However, we also used their provided checkpoint and evaluated its performance on the PCBA dataset. It could be concluded that LigUnity trained on its full dataset leads the zero-shot performance, which also highlights the value of larger training datasets, similar to Table 3. When constrained to PDBBind alone, our approach outperforms LigUnity across most metrics, achieving an AUC of 57.77% and $\text{EF}_{0.5\%}$ of 7.01. These results strongly demonstrate its

Table 6: **Zero-shot Virtual Screening on LIT-PCBA**. Baseline results are from Gao et al. (2023); Feng et al. (2025); Jia et al. (2024). Models with * are trained with PDBBind data only. Bold numbers indicate the best performance.

	AUC (%) ↑	BEDROC (%) ↑	EF ↑ 0.5%	EF ↑ 1%	EF ↑ 5%
Surflex	51.47	-	-	2.50	-
Glide-SP	53.15	4.00	3.17	3.41	2.01
Planet	57.31	-	4.64	3.87	**2.43**
Gnina	60.93	5.40	-	4.63	-
DeepDTA	56.27	2.53	-	1.47	-
BigBind	60.80	-	-	3.82	-
DrugCLIP *	58.15	4.12	4.11	3.08	2.27
LigUnity *	57.61	4.34	4.06	3.03	2.25
Ours *	**57.77**	**6.27**	**7.01**	**5.20**	2.18

Table 7: Zero-shot Virtual Screening on DEKOIS.

	AUC (%) ↑	BEDROC (%) ↑	EF ↑ 0.5%	EF ↑ 1%	EF ↑ 5%
LigUnity	76.92	47.20	**18.57**	16.25	8.21
Ours	**81.05**	**47.71**	18.085	**16.77**	**8.74**

robustness under limited training data and the effectiveness of our efficient tokenization strategy. In addition, we also provides comparison with LigUnity following (Feng et al., 2025) in Table 7 and 8. These results validate that h-MINT generalizes effectively across datasets and tasks, including both affinity-ranking and virtual-screening benchmarks.

To demonstrate the significance of our results, we conducted statistical significance tests for all benchmarks (DUDE, PCBA, DEKOIS, and FEP). For all comparisons between h-MINT(ours) vs. LigUnity, we obtained p-values < 0.005, demonstrating that the improvements are statistically significant and consistent, rather than due to random variation.

C.5 Ablation of MSE Loss over LigUnity

To isolate the contribution of this loss, we trained LigUnity with additional MSE loss (exact same combined loss as ours) under identical settings on the PDBBind training set, as shown in Table 9. The results on DUDE and LIT-PCBA are shown in the table above, which confirms the following findings: (i). Effect of the proposed auxiliary loss. Using our proposed auxiliary loss consistently improves LigUnity across almost all metrics on both datasets. For example, on DUDE, AUC improves from 81.69 to 82.57, and BEDROC from 46.01 to 47.58. On LIT-PCBA, early-recognition metrics show noticeable gains as well. This confirms that additional loss is beneficial and strengthens the model's scoring ability. (ii). Advantage of h-MINT (LigUnity+MSE vs Ours). Our model further improves over LigUnity+MSE on most metrics. Gains are particularly clear in early-recognition measures such as BEDROC and EF0.01, which are widely regarded as key metrics for virtual screening. These results confirm that: our proposed regression loss is effective, but our h-MINT architecture delivers additional, consistent boosts beyond what the regression loss alone can offer. Thus, the comparison with LigUnity is fair, and the observed improvements come from both components of our method.

Table 8: Zero-shot Virtual Screening on JACS/Merck.

	r^2
LigUnity	0.173
Ours	**0.216**

Table 9: Ablation of MSE Loss over LigUnity

Dataset	Model	AUC (%) ↑	BEDROC (%) ↑	EF ↑ 0.5%	EF ↑ 1%	EF ↑ 5%
DUDE	LigUnity	81.69	46.01	34.44	29.07	10.26
	LigUnity+MSE	82.57	47.58	**35.83**	29.77	10.70
	Ours	**84.47**	**47.65**	35.06	**29.90**	**10.76**
LIT-PCBA	LigUnity	57.61	4.34	4.07	3.04	**2.26**
	LigUnity+MSE	57.68	5.64	6.50	4.22	2.14
	Ours	**57.77**	**6.21**	**7.01**	**5.20**	2.18

Table 10: Vocabulary Statistics on LBA training set.

min_freq	# tokens (basic / composite / all)	avg token size (basic / composite / all)
200	41 / 52 / 93	2.56 / 5.81 / 4.38
100	54 / 80/ 134	2.87 / 6.53 / 5.05
50	74 / 137 / 211	3.11 / 7.44 / 5.92
20	94 / 200 / 294	3.28 / 8.11 / 6.56
10	112 / 400 / 512	3.54 / 9.55 / 8.23

C.6 Computational Overhead

OverlapBPE duplicates certain atoms during tokenization to maintain the continuity and integrity of chemical substructures. Because of these overlapping tokens, the final number of atoms becomes roughly 1.32 times the original. Despite this, both tokenization and graph construction are highly parallelizable and can be performed fully offline in preprocessing. In practice, the overhead is negligible: OverlapBPE only takes 7 minutes to process 47.9k molecules using 32 CPUs for virtual screening training data.

During training and inference, the main computational cost comes from the underlying UniMol encoder. h-MINT functions as a light-weight adapter, and the runtime difference compared with LigUnity is minimal: our's training time is $\times 1.12$ than LigUnity, and our's inference time is $\times 1.07$ than LigUnity. Therefore, although h-MINT introduces a richer atom-fragment representation, the parallel and offline preprocessing ensures that the runtime during the actual virtual screening pipeline remains nearly unchanged.

D Additional Analysis and Experiments

D.1 Vocabulary Statistics

We provide vocabulary statistics on LBA training set in Table 10. For all the datasets, we extract vocabularies solely from the training set, without introducing additional data.

D.2 Representing Chirality for HTS

We evaluate whether explicitly encoding stereochemistry in our fragment representation improves early enrichment on eight PubChem HTS assays. In contrast to structure-based virtual screening in Section 4.2, HTS assay data do not include explicit target information. Each assay contains active and inactive compounds corresponding to the same target. We construct two OverlapBPE vocabularies: (*i*) *Ours-non-chiral*, which omits stereochemical markers, and (*ii*) *Ours-chiral*, which operates on 2D graphs augmented with 3D conformer cues (used only to disambiguate stereocenters) and assigns isomeric SMILES identifiers to tokens, thereby preserving R/S and `@`/`@@` annotations. Each molecule is tokenized into overlapping fragments; we compute sparse bag-of-tokens features and train an XGBoost logistic classifier per assay on the official train/valid/test split. We report $\text{logAUC}_{[0.001,0.1]}$, which emphasizes the low false-positive region relevant to early enrichment.

Table 11: Ablation Study of OverlapBPE and h-MINT on LBA.

	RMSE ↓	Pearson ↑	Spearman ↑
GET	1.331 ± 0.008	0.618 ± 0.005	0.607 ± 0.005
GET+PS	1.312 ± 0.016	0.631 ± 0.011	0.642 ± 0.011
h-MINT+PS	1.321 ± 0.010	0.633 ± 0.007	0.641 ± 0.008
GET+OverlapBPE	N/A	N/A	N/A
Ours (h-MINT+OverlapBPE)	**1.276 ± 0.011**	**0.660 ± 0.001**	**0.661 ± 0.001**

D.3 Ablation Study of OverlapBPE and h-MINT

OverlapBPE tokenization and overlap-compatible hierarchical interaction model, jointly form an integrated framework to tackle the challenge of fuzzy boundaries of meaningful molecular substructures in 3D molecular interaction modeling. Meaningful comparison can only be made when they're used together, because (i) no other network architectures are available for overlapping substructures, and (ii) when non-overlapping tokenization is used, the molecular graphs for h-MINT and GET become identical. As evidence, we provide the following ablation on LBA dataset that adopts non-overlap PS tokenizer for h-MINT in Table 11.

As can been seen in this table, GET is not compatible with OverlapBPE. OverlapBPE+hMINT consistently outperforms models with PS tokenizer, demonstrating a clear gain of OverlapBPE. When non-overlap PS tokenizer is used, GET+PS and h-MINT+PS achieve similar performance as expected. The tokenizer and h-MINT architecture are both necessary to handle overlapping fragments and preserve key chemical information (atomic integrity, ionic states, chirality).

D.4 Noise-Robustness Analysis

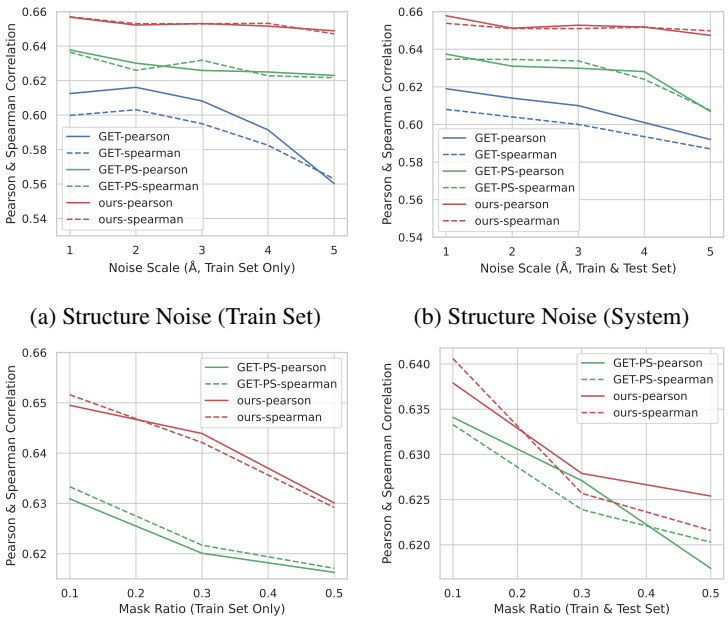

(a) Structure Noise (Train Set) (b) Structure Noise (System)

(c) Fragment Mask (Train Set) (d) Fragment Mask (System)

Figure 6: **Noise robustness comparison on LBA**. We report results from 3 runs.

In this section, we analyze the robustness and generalization of GET, GET-PS, and our model under different noise scales on LBA. We consider two noise settings: adding noise only to the training set for simulating scenarios when training data is of low quality or is predicted, and adding noise to both training and test sets for simulating system bias or data resolution. To investigate the effect of noise in different features, we add random noise to input structures, or randomly mask token types with

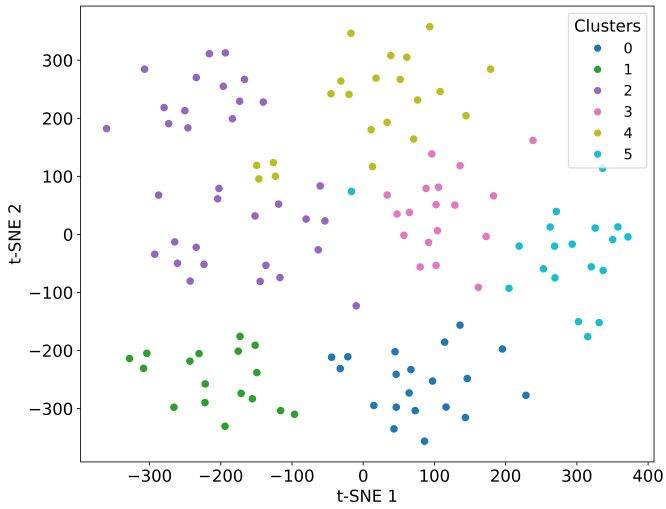

Figure 7: **t-SNE Visualization of Fragment Embeddings.**

some ratio[7]. The results can be found in Figure 6. In general, we can conclude that: (i) Our model is robust to structure noise even up to 5 Å. (ii) Compared with atom-level 3D structures, token types provide stronger inductive bias for binding affinity prediction, which again highlights the importance of fragment-level representations.

D.5 Fragment Embedding Analysis of h-MINT

To evaluate the representation capability of the h-MINT model for molecular fragments, we first analyzed the spatial distribution of fragment embeddings using t-SNE, shown in Figure 7. The results showed that all fragments clustered into 6 distinct categories in the latent space.

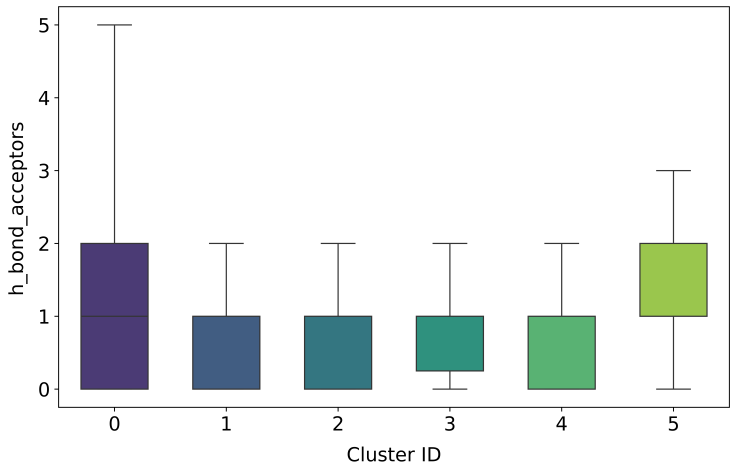

Figure 8: **H-bond acceptors distribution across clusters.**

Statistical analysis of fragments in each cluster, as shown in Figure 8, revealed that Cluster 5 exhibited significant chemical specificity. This cluster was predominantly enriched with functional groups containing lone electron pairs on `N` and `O` atoms, such as `C=O`, `CNC(C)=O`, and `CNS(=O)(=O)`.

[7]Since GET only uses atom representations for molecules, we only compare GET-PS with ours in (c)-(d).

These structures, acting as typical hydrogen bond acceptors, can form stable interactions with polar amino acids (e.g., the hydroxyl group of serine or the guanidinium group of arginine) in protein binding pockets. This ability to capture key chemical features enables h-MINT to more sensitively identify structural determinants affecting binding affinity, leading to superior performance over existing sequence- or graph-based baseline models on the binding affinity prediction and virtual screening tasks.

D.6 Effect of the frequency threshold

We vary the minimum frequency used by OverlapBPE, yielding vocabularies of sizes {98, 136, 212, 294}. Performance improves from small vocabularies to around 200, where we observe the best aggregate results, and then slightly degrades at 294. Run-to-run variation is small (std < 0.006 across metrics), indicating stable behavior. These trends suggest a bias–variance trade-off: overly strict thresholds (very small vocab) underfit by missing informative fragments, whereas overly lax thresholds (very large vocab) admit rare or redundant fragments that increase sparsity and noise. A moderate threshold around 200 offers the best balance between coverage and denoising.

Table 12: **Vocabulary size ablation on PDBBind**. Values are obtained over three runs.

Vocab size	Pearson	Spearman	RMSE
98	0.618 ± 0.005	0.601 ± 0.006	1.344 ± 0.007
136	0.615 ± 0.002	0.605 ± 0.002	1.332 ± 0.003
212	0.640 ± 0.004	0.626 ± 0.005	1.299 ± 0.001
294	0.622 ± 0.002	0.617 ± 0.003	1.327 ± 0.002

D.7 Additional Experiments on Molecular Property Prediction

We include 3 property prediction tasks from MoleculeNet. The baseline follows MoleculeNet directly, which extracts ECFP features and trains XGBoost with grid search. The ECFP features are chosen from 128-bit, 512-bit, 1024-bit and 2048-bit according to dataset. We augment the ECFP features with bag-of-word features extracted from OverlapBPE and train the same XGBoost. The results are in Table 13. The significant improvements in prediction error confirm that OverlapBPE provides discriminative representations for molecules.

Table 13: Molecular Property Prediction Benchmarks from MuleculeNet.

RMSE	ESOL ↓	FreeSolv ↓	Lipo ↓
ECFP	1.5668	3.9498	0.8875
ECFP + OverlapBPE	**1.2972**	**3.3409**	**0.8270**

D.8 Example Tokens and Chemical Insights

By construction, OverlapBPE induces a hierarchical organization of fragments: basic tokens correspond to chemically primitive units (atoms, bonds, individual rings), while composite tokens capture larger patterns such as fused ring systems and side chains. In this section, we analyze how the learned fragments align with standard functional chemistry.

We provide a list of the top 100 fragments mined from the LBA training set in Fig. 9, and we are able to obtain many chemically and biologically meaningful subunits or motifs. We emphasize that this motif-mining procedure is fully automatic, based solely on the data distribution, and leverages no prior chemical or biological knowledge. We analyse and categorize the mined fragments into the following chemically or biologically meaningful parts.

Chemical functional groups. A functional group is a specific group of atoms or bonds within a molecule that is responsible for its characteristic chemical properties and reactions. Representative functional groups mined include: *carboxyl, phosphate, amide (peptide bond), benzyl, secondary*

amino, tertiary amino, and quaternary amino (ammonium). These functional groups are small chemical subunits that were often selected by hand in previous functional-group-based tokenization but can be easily recovered with our approach.

Biomolecule subunits. Compared to simple chemical functional groups, biomolecules such as proteins, DNA, RNA, and polysaccharides are significantly larger. Yet, the monomers that constitute these biomolecules exhibit characteristic patterns, such as amino acids, nucleotides, and saccharides. Indeed, we observe a considerable number of biologically meaningful fragments in our codebook: *peptide bond, adenine, pyranose, deoxyribose*, and, most notably, the whole nucleotide *adenosine* monophosphate, which consists of an adenine, a ribose, and a phosphate. To the best of our knowledge, none of the existing fragmentation approaches has been able to mine such large subunits while preserving their biological significance.

Drug subunits. Remarkably, we also observed that our approach could mine large chemical subunits that are common motifs in small-molecule drugs. These include: *adamantane*, a 10-carbon tricyclic motif with a highly symmetric fused four hexane rings, occurring in some antiviral drugs; *sulfonamide*, in the antibacterial drug sulfanilamide; and most notably, the 28-heavy atom *sulfonamide protease inhibitor motif* in HIV drugs. Indeed, our approach automatically mined this large subunit, demonstrating its effectiveness at capturing the biochemical roles of many motifs.

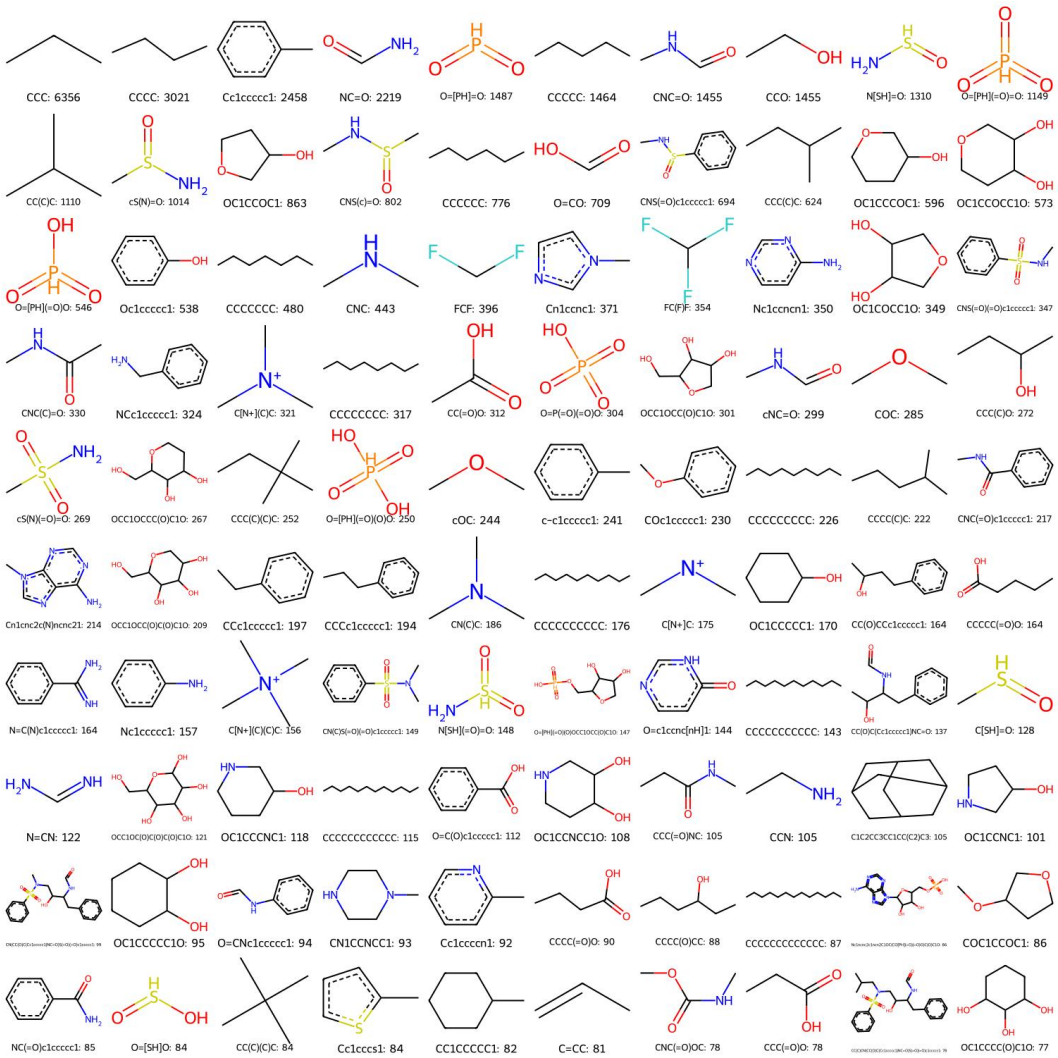

Figure 9: Top-100 composite tokens from LAB vocabulary.

E THE USE OF LARGE LANGUAGE MODELS

We employ large language models exclusively for language editing, which is limited to polishing text to improve readability. No language models contributed to the development of research ideas, analysis, models, or interpretation of results.